CO_2-to-methanol electroconversion on a molecular cobalt catalyst facilitated by acidic cations

Sunmoon Yu[1]*, Hiroki Yamauchi[2], Shuo Wang[1,3], Abhishek Aggarwal[1,3], Junghwa Kim[1,3], Botao Huang[1], Hongbin Xu[1,3], Daniel J. Zheng[1,3], Xiao Wang[1,4], Haldrian Iriawan[1,3], Davide Menga[1], Yang Shao-Horn[1,3,5]*

Affiliations:

[1]Research Laboratory of Electronics, Massachusetts Institute of Technology; Cambridge, MA 02139, USA

[2]Scientific Research Laboratory, Niterra Co., Ltd; Iwasaki, Komaki, Aichi, 485-8510, Japan

[3]Department of Materials Science and Engineering, Massachusetts Institute of Technology; Cambridge, MA 02139, USA

[4]Department of Chemical Engineering, Massachusetts Institute of Technology; Cambridge, MA 02139, USA

[5]Department of Mechanical Engineering, Massachusetts Institute of Technology; Cambridge, MA 02139, USA

*Corresponding author. Email: sunmoon@mit.edu, shaohorn@mit.edu

Abstract:

The crucial role of electrolyte cations in CO_2 electroreduction has received intensive attention. One prevailing theory is that through electrostatic interactions or direct coordination, larger cations such as Cs^+ can better stabilize the key intermediate species for CO and multicarbon (C_{2+}) product generation, for example, on silver and copper, respectively. Herein, we show that smaller, more acidic alkali metal cations greatly enhance CO_2-to-methanol conversion kinetics ($Li^+ > Na^+ > K^+ > Cs^+$) on an immobilized molecular cobalt catalyst, unlike the trend observed for CO and C_{2+}. Through kinetic isotope effect studies and electrokinetic analyses, we found that hydration shell of a cation serves as a proton donor in the rate-determining protonation step of adsorbed CHO where acidic cations promote the proton-coupled electron transfer. This study reveals the promotional effect of cation solvation environment on CO_2 electroreduction beyond the widely acknowledged stabilizing effect of cations.

Main Text:

Non-innocent role of electrolyte cations in electrocatalytic reactions has recently attracted tremendous research interests, spanning from hydrogen evolution/oxidation reactions, relatively simple two-electron/proton transfer reactions[1-3], to more complex electrochemical CO_2 reduction reaction (CO_2RR) involving multiple electron/proton transfers[4-6]. Non-covalent interactions between cations, interfacial water molecules, and reactants/intermediate species in the catalytic microenvironment have shown to greatly affect intrinsic reactivity and selectivity of catalytic sites beyond what is typically determined by covalent bonding between the reaction site and an adsorbate. For instance, Hori et al. have reported in their seminal CO_2RR study that ethylene selectivity on a polycrystalline copper surface increases with the increase of alkali metal cation size in bicarbonate electrolyte ($Li^+ < Na^+ < K^+ < Cs^+$)[7]. Since then, many reports have supported the trend that larger cations generally promote CO_2RR while suppressing hydrogen evolution[1,4,8], a competing side reaction under CO_2-reducing conditions.

To account for the cation effect on catalytic CO_2RR activity, several theoretical explanations have been proposed, which include electric field effect[6,9,10] and cation coordination[4,5], both stabilizing key intermediate species through medium- and short-range electrostatic interactions in a rate-determining step (RDS), respectively. The key intermediates, for example, include anionic CO_2 adsorbate ($*CO_2^-$) after an initial electron transfer to CO_2 on silver for CO_2-to-CO conversion[11], and adsorbed anionic CO dimer ($*OCCO^-$) after symmetric coupling of adsorbed CO on copper, accompanying an electron transfer, for CO_2-to-C_{2+} conversion[5,12,13]. Larger cations with a weakly bound hydration shell can accumulate at the electrified interface and more effectively stabilize these negatively charged key intermediates than smaller cations[4,5]. However, the potential role of cations in proton-coupled electron transfer (PCET) steps during CO_2RR have not been adequately examined, where different steps can be rate-limiting for various reaction products including methanol[14]. Specifically, non-covalent interaction of cations with surrounding water molecules and its impact on the PCET steps during CO_2RR have not received due attention despite its potential significance.

In the present study, we investigated the catalytic role of electrolyte cations for electrochemical CO_2-to-methanol conversion on a molecular cobalt catalyst, which involves total six electron transfers while water serves as a proton donor in neutral pH conditions:

$$CO_2 + 6e^- + 5H_2O \rightarrow CH_3OH + 6OH^-$$

Cobalt phthalocyanine (CoPc) was employed as a model catalyst (Fig. 1a), since it has not only a well-defined structure (i.e., a cobalt single atom coordinated by four nitrogen atoms) but also has the capability of selective CO_2-to-methanol electroconversion beyond two-electron reduction of CO_2 to CO[15-17]. Theoretical studies on molecular cobalt catalysts have suggested that a protonation step after CO adsorbate formation could be the RDS for methanol generation[18,19]. Thus, we reasoned that if the RDS involves a PCET, cations and their solvation environment must have non-negligible influence on the PCET kinetics, since a proton transfer should occur from the interfacial water molecules, which non-covalently interact with a cation nearby, to an intermediate species bound on the cobalt site[20,21]. Consequently, this could affect catalytic activity for methanol production.

CoPc monomers were well dispersed on carbon nanotubes (CoPc/CNT), confirmed by electron microscopy and spectroscopy (Fig. 1b and Supplementary Figs. 1 and 2). CoPc/CNT loaded on a carbon support was tested for 1 hour in a typical H-cell for electrochemical CO_2RR in

a wide range of potentials with various alkali metal cations in a bicarbonate solution (Fig. 1c and Supplementary Fig. 3). Gas and liquid products were analyzed using gas chromatography (GC) and proton nuclear magnetic resonance (^{1}H NMR) spectroscopy, respectively. In the potential region more positive than –0.7 V versus reversible hydrogen electrode (V_{RHE}), CO is the major product[22,23], where the CO activity and selectivity exhibit less sensitivity to the cation identity in comparison to that of silver (Supplementary Fig. 4). CoPc/CNT can selectively produce CO in the presence of various cations (Supplementary Fig. 5), achieving up to ~90% CO selectivity, where larger alkali metal cations result in larger CO partial current density in this potential region (Supplementary Fig. 5). In the high overpotential region (<–0.7 V_{RHE}), CoPc/CNT begins to produce methanol from CO_2RR, but surprisingly, it shows an opposite cationic trend ($Li^+ > Na^+ > K^+ > Cs^+$) for methanol selectivity compared to the trend observed at all potentials for CO production ($Li^+ < Na^+ < K^+ < Cs^+$). As both CO and methanol from CO_2RR are known to share the same CO intermediate (CO_{int})[12,14], the promotion of CO generation by larger cations (i.e., a higher CO faradaic efficiency) but not methanol selectivity suggests a different RDS for methanol production (Fig. 1c and Supplementary Fig. 6). Further support came from $^{13}CO_2$RR and control experiments, validating that methanol was generated from electrochemical CO_2RR by CoPc (Fig. 1c inset and Supplementary Figs. 7–9).

To assess how cations affect CO intermediate formation and CO_2RR selectivity, we compared the generation rate (nmol/s) of CO_{int} in the bicarbonate electrolyte with different cations (Fig. 2a). This generation rate of CO_{int} was derived from CO_2RR product partial currents (CO and methanol) (Supplementary Figs. 10 and 11), which is more appropriate in evaluating the catalytic role of cations in CO_2-to-CO_{int} conversion than comparing partial currents to produce CO and methanol due to different numbers of electron transferred (two and six, respectively). In the high overpotential region, larger cations lead to higher CO_{int} generation rates and selectivity compared to smaller cations (Fig. 2a,b), presumably due to better stabilization of its key intermediate, namely $*CO_2^-$, by the larger cations. Nonetheless, smaller cations enhance the kinetics of CO_{int}-to-methanol conversion, increasing further reduction of CO_{int} and resulting in higher partial current densities toward methanol (Fig. 2c,d). This cation-dependent catalytic activity for methanol production signifies that electrolyte cations play a critical role beyond its stabilizing role in CO_2 activation and subsequent CO_{int} formation[4,5].

That cation identity greatly affects the methanol production rate (Fig. 2c) strongly suggests proton source is associated with the cation species in the vicinity of catalytic active site. In addition, given that a near-neutral condition (pH 6.8) and high overpotentials were used where an elevated interfacial pH is expected, water is likely the major proton source for CO_2RR rather than bicarbonate (Supplementary Fig. 12)[24-26]. These results lead us to postulate that water molecules associated with electrolyte cations serve as a proton donor for CO_2-to-methanol conversion on CoPc catalyst and thus a proton transfer from the interfacial water molecules with a concomitant electron transfer to an intermediate species pertains to the overall rate of methanol production. Therefore, the proton transfer kinetics are expected to be regulated by the extent of non-covalent interaction between electrolyte cation and surrounding water molecules.

To elucidate the role of protons in methanol production, we conducted kinetic isotope effect (KIE) studies. KIE studies of aqueous electrocatalytic processes have protons in the electrolyte substituted with deuterons to probe if a proton is involved in the RDS, pursuing mechanistic understanding[27-29]. In our study, deuterated electrolyte (0.1 M $LiDCO_3$) was used in place of protic counterpart (0.1 M $LiHCO_3$), where the magnitude of KIE was measured at different

applied potentials. The KIE value was determined by the ratio of partial current density of a reaction product in protic condition ($j_{product}^{H}$) to that in deuterated condition ($j_{product}^{D}$). First of all, at –0.6 V_{RHE}, where CO is the only CO_2RR product, CO partial current (j_{CO}) remains comparable in deuterated, protic, and D_2O-H_2O mixture electrolytes (Fig. 3a). This result indicates that proton is not involved in the RDS of CO_2-to-CO conversion and does not affect its kinetics[30]. In contrast, total hydrogen evolution current (j_{H2} and j_{D2}) increases with the decreasing fraction of D_2O (while increasing fraction of H_2O) in the mixed electrolytes due to faster proton discharge from H_2O than D_2O (i.e., faster water dissociation)[29], supporting a proton transfer step as the RDS (Fig. 3a and Supplementary Fig. 13a).

We further performed CO_2-to-methanol conversion in the high overpotential range (<–0.7 V_{RHE}) using the deuterated electrolyte, where CO, D_2, and CD_3OD were the reaction products. The deuterated methanol product was measured using deuterium NMR (^{2}H NMR) spectroscopy (Supplementary Fig. 14). While the overall CO_{int} generation rates, derived from CO and methanol partial currents, are not affected by the proton donor identity ($g_{COint}^{D} \sim g_{COint}^{H}$) at the high overpotentials (Fig. 3b), CO partial current density in the deuterated electrolyte surpasses that in the protic electrolyte ($j_{CO}^{D} > j_{CO}^{H}$) (Supplementary Fig. 13b). In contrast, methanol partial current density in deuterated electrolyte decreases by about 6.5 times compared to that in the protic electrolyte ($j_{CD3OD}^{D} < j_{CH3OH}^{H}$) (Fig. 3c). Hence, this notable KIE and the inefficient CO_{int}-to-methanol conversion (Fig. 3d) in the deuterated electrolyte confirm that proton is involved in the RDS of CO_2-to-methanol conversion.

To get more mechanistic insights into the reaction pathway of CO_2RR on CoPc catalyst, Tafel analyses were conducted (Fig. 4). For CO_2-to-CO conversion, an average Tafel slope of 139±5 mV/dec was obtained (Fig. 4c), which did not change much depending on the cation identity nor the type of aqueous solvent (D_2O or H_2O) (Supplementary Fig. 15). Previous studies have reported that an electron transfer to CO_2 is the RDS for CO_2-to-CO conversion on CoPc[18,31], having a Tafel slope of 120 mV/dec, if a symmetry factor (β) of 0.5 is assumed (Supplementary Note). Together with the KIE result on CO generation, our Tafel analysis result also supports that the CO_2 activation step involving an electron transfer is the RDS for CO_2-to-CO conversion.

For CO_2-to-methanol conversion, the cation identity neither affects the onset potential for methanol production (about –0.7 V_{RHE}, Fig. 4a), nor influences the Tafel slope (40±4 mV/dec) (Fig. 4d and Supplementary Fig. 16), where the electrolyte cations only regulate the reaction kinetics. Since CO_{int} is a branching point at high overpotentials, leading to CO and methanol as final products, the RDS should be a PCET step after *CO formation, which is supported by previous theoretical studies on cobalt-based molecular catalysts[18,19]. Although the measured Tafel slope agrees well with a case where protonation of *CHO is the RDS (Supplementary Fig. 4d), the fact that multiple intermediates can be involved from CO_2 up to an RDS and their coverages are also potential dependent[32,33] makes it challenging to identify the RDS solely from the Tafel analysis of CO_2-to-methanol conversion (Supplementary Note).

We therefore conducted CO reduction reaction (CORR) (Fig. 4, and Supplementary Figs. 17 and 18), as *CO is an important intermediate for methanol production[16]. A similar cation dependence ($Li^+ > Na^+ > K^+ > Cs^+$) for CORR kinetics in alkaline electrolyte (pH 13) was observed as that of CO_2RR (pH 6.8). This similar trend corroborates that water molecules associated with cations are the proton donors for methanol production. Meanwhile, lower methanol partial currents in CORR than CO_2RR (Fig. 4a) could be due to a lower solubility of CO (1 mM) than that of CO_2 (34 mM) in aqueous electrolyte[25].

Importantly, there is a considerably positive shift in potential on the RHE scale for methanol production from CORR (>200 mV, Fig. 4a), while the methanol partial currents from CO_2RR and CORR and their onset potentials do not overlap with one another, when replotted based on the standard hydrogen electrode (SHE) scale (Fig. 4b). This potential shift on the RHE scale and potential mismatch on the SHE scale was previously observed for methane production on polycrystalline copper catalysts, while absent for multicarbon products[25,34]. This observation was attributed to a rate-determining proton-electron transfer step, with water molecule as a proton donor, occurring later than the protonation of CO[14,25,35]. Therefore, these results reinforce that water molecules in the hydration shell of a cation is the major proton donor and the CO protonation step is not the RDS for methanol generation.

In addition, the average Tafel slope measured for CORR with different cations was 47±5.5 mV/dec (Fig. 4e and Supplementary Fig. 19), much lower than 120 mV/dec, an expected value with the protonation of CO as the RDS[25,35]. This result clearly rules out the possibility of proton-electron transfer to *CO to form an adsorbed formyl (*CHO) as the RDS. Instead, our Tafel analyses for both CO_2- and CO-to-methanol conversion (Fig. 4d,e), where different elementary steps were considered for the RDS, consistently support a PCET to *CHO to generate formaldehyde[36] as the RDS, agreeing well with experimentally measured Tafel slopes (see Supplementary Notet for more detailed discussion).

For hydrogen evolution reaction (HER) during CO_2RR, CNT support itself contributes to the H_2 partial current (Supplementary Fig. 11c), and it shows nearly constant currents in the presence of different cations over the low overpotential region (>–0.7 V_{RHE}). The corresponding infinite Tafel slope suggests that a rate-limiting chemical step, for example, the Tafel step, controls HER on CNT (Supplementary Fig. 20). At high overpotentials (<–0.7 V_{RHE}), CoPc begins to contribute more to the H_2 partial current. Since it has a single reaction site, the RDS could be either the Volmer or the Heyrovsky step (Supplementary Fig. 20e)[18,37]. More importantly, a cation dependence trend similar to that for methanol production kinetics was observed for HER kinetics ($Li^+ > Na^+ > K^+ > Cs^+$) (Supplementary Fig. 5c). This result along with KIE on HER (~6.5, Supplementary Fig. 13c) further supports that the hydration shell of cations might also serve as a proton donor for hydrogen generation on CoPc under CO_2RR conditions. The higher acidity of smaller cations likely permits more facile water dissociation due to their stronger cation-water interactions (i.e., M^+–O_{water}), lowering the proton transfer energy barrier to the cobalt active site and consequently increasing HER activity[20,21,38].

Combining the experimental results, a complete catalytic cycle of CoPc catalyst is described in Fig. 5a. For CO_2-to-CO conversion, CO_2 activation with an electron transfer is the RDS (Fig. 5b), which is supported by the absence of KIE and the Tafel analysis. On the other hand, for CO_2-to-methanol conversion, a proton-electron transfer to *CHO is the RDS (Fig. 5c), based on the notable KIE observed and the Tafel analyses in CO_2 and CO electroreduction. We also performed density functional theory (DFT) calculations on CO_2-to-methanol conversion energetics (Fig. 5d and Supplementary Figs. 21–23) and found that the protonation of *CHO has a much higher energy (0.42 eV) than that of the *CO protonation step (0.04 eV) at the equilibrium potential (0.02 V_{RHE}), supporting our conclusion. Furthermore, we carried out crystal orbital Hamilton populations (COHP) analysis to compare the interaction between CoPc and intermediates through the Co-C bond[39,40], and found that CoPc-CH_2O shows a very weak bonding state compared to CoPc-CO and -CHO, rationalizing the large energy gap for the *CHO

protonation step (Supplementary Fig. 24). At –0.7 V_{RHE}, the experimental onset potential, CO_2-to-methanol conversion becomes energetically downhill (Fig. 5d), allowing methanol production.

The cation dependency on methanol production signifies that water molecules in the hydration shell of a cation in the vicinity of a cobalt single site are proton donors, and thus, similarly to HER, the proton transfer kinetics of the water molecules is greatly affected by the non-covalent interaction between the water and the electrolyte cation. Evident from the radial distribution function plots obtained from molecular dynamics (MD) simulations, stronger association of water molecules with smaller cations was observed (Supplementary Fig. 25). In addition, we found that larger cations tend to approach the *CHO intermediate (e.g., M^+–O_{*CHO}) more easily than smaller ones owing to their weakly bound solvation shell and water-structure-breaking property[1,41] (Fig. 5e and Supplementary Figs. 26 and 27). An important implication is that smaller cations tend to have a greater availability of water molecules in the vicinity of *CHO (Fig. 5f). Moreover, acidic cations such as Li^+ with a large hydration energy (namely, strong cation-water interactions) and a weaker O–H bond[21] can provide protons more readily from their hydration shell to the key intermediate (*CHO), relaying protons from bulk electrolyte to the electrified interface. Consequentially, acidic cations can enhance the CO_2-to-methanol conversion kinetics.

In summary, this study elucidates the mechanistic pathway for electrocatalytic CO_2-to-methanol conversion on a cobalt single reaction site, identifying the rate-limiting step. This work further uncovers the dual roles of cations during CO_2RR to methanol: (1) stabilizing effect on the key intermediate species for CO_2-to-CO conversion and (2) promoting effect on the proton-electron transfer for the further reduction to methanol. Our findings demonstrate that cation solvation environment regulates PCET kinetics during CO_2RR, and it can be modified to improve catalytic activity for methanol production, exemplified by the increase in partial current with smaller electrolyte cations ($Li^+ > Na^+ > K^+ > Cs^+$) (Supplementary Fig. 28). Manipulating non-covalent interactions among multiple species in the catalytic microenvironment including electrolyte cations, interfacial water molecules, and reaction intermediates holds great potential as an approach to guide electrocatalytic CO_2RR, especially for products involving a rate-limiting PCET step, and also other electrocatalytic processes in aqueous conditions. Especially, understanding such non-covalent interactions involving a single active site (e.g., single-atom catalysts) is an important area for future studies.

Methods:

Electrode preparation

Catalyst ink and electrode were prepared following the procedure described in a previous report with some modifications[15]. As-received multi-walled carbon nanotubes (CNTs, >98% carbon basis, Sigma-Aldrich) was calcined at 500 °C for 1 hour under ambient atmosphere. The calcined CNTs were transferred to a centrifuge tube containing 5 wt.% HCl solution and sonicated for 30 mins, after which it was stirred at 700 rpm overnight. The purified CNTs were repeatedly washed with deionized water and centrifuged (12,000 rpm for 10 mins) multiples times until pH becomes neutral. The CNTs were dried in a freeze dryer (Labconco FreeZone 2.5 plus).

For catalyst preparation (CoPc/CNT), 30 mg of the purified CNTs was dispersed in 20 ml of dimethylformamide (DMF, HPLC grade, ≥99.9%, Sigma-Aldrich), while 1.5 mg of cobalt phthalocyanine (CoPc, Thermo Fisher Scientific) was dispersed in 10 ml of DMF. After 30 mins of sonication, two solutions were mixed, and its mixture was sonicated for another 30 mins. The

mixed solution was stirred at 700 rpm for 24 hours and centrifuged twice at 12,000 rpm for 10 mins each. The precipitate was washed with DMF and ethanol, and centrifuged, respectively, and dispersed in 10 ml of deionized water before freeze drying. For bare CNT control sample, identical procedure was used without adding CoPc.

To make catalyst ink, 8 mg of CoPc/CNT was added to 2 ml of absolute ethanol along with 24 μl of Nafion solution (5 wt.%, Sigma-Aldrich). For complete dispersion, the ink was sonicated for at least 2 hours. To prepare electrodes for electrochemical testing, total 100 μl of the catalyst ink was drop casted using a pipette on a carbon paper (Sigracet 29AA, Fuel Cell Store) with 1 cm^2 geometric active area (catalyst mass loading: 0.4 mg/cm^2_{geo}).

For polycrystalline foil testing (0.1 mm thick, Thermo Fisher Scientific), as-received silver foil (99.998%) and cobalt foil (99.995%) were cut into pieces with 1 and 0.3 cm^2 geometric active area, respectively, and mechanically polished using a sandpaper (400 grit, 3M), and thoroughly rinsed with ethanol and deionized water before each experiment.

Electrochemical testing

All electrochemical testing was conducted in an H-cell type electrochemical cell where two compartments were separated by an anion exchange membrane (Selemion, DSVN, Bellex International Corp.). Platinum foil was used as a counter electrode while Ag/AgCl 3M KCl was used as a reference electrode.

Electrolytes for CO_2 reduction reaction (CO_2RR) were prepared by purging 0.05 M carbonate solution with CO_2 gas (Airgas, Research Grade) overnight and pH was measured (~6.8). Carbonate salts used in this study are Li_2CO_3 (99.999%, Sigma-Aldrich), Na_2CO_3 (99.998%, Thermo Fisher Scientific), K_2CO_3 (99.997%, Thermo Fisher Scientific), and Cs_2CO_3 (99.995%, Sigma-Aldrich). For bicarbonate concentration dependence experiment, Li_2SO_4 (99.99%, Sigma-Aldrich) was used as a supporting electrolyte. For organic cations, tetramethylammonium hydroxide (TMAOH, 25 wt.%, 99.9999%, Thermo Fisher Scientific) was first converted to bicarbonate solution by purging with CO_2 gas and diluted to make 0.1 M bicarbonate solution. For deuterated electrolyte preparation, deuterium oxide (99.9 at.% D, Sigma-Aldrich) was used instead of deionized water (18.2 MΩ·cm, Milli-Q Direct Water Purification System). Prior to each electrocatalytic testing, electrolyte was saturated with CO_2 gas, and the gas flow was kept at 20 sccm (standard cubic centimeters per minute) with continuous stirring during CO_2 electrocatalysis.

For CO reduction reaction (CORR) experiment, hydroxide electrolytes were used for testing and prepared by using LiOH (99.995%, Thermo Fisher Scientific), NaOH (99.99%, Sigma-Aldrich), KOH (99.99%, Sigma-Aldrich), and $CsOH{\cdot}H_2O$ (99.95%, Sigma-Aldrich). Before testing, electrolyte was purged with CO (Airgas, ultra-high purity) for 30 mins at 20 sccm and kept bubbled during the electrolysis. For electrocatalytic testing, potentiostatic experiments were performed for typically 65 mins, and electrode potentials were converted to the reversible hydrogen electrode (RHE) scale using the following equation: E (versus RHE) = E (versus Ag/AgCl 3 M KCl) + 0.210 + 0.0591 × pH. For ohmic loss compensation, solution resistance was measured at the end of each testing and *iR* drop was manually compensated.

In the kinetic isotope effect (KIE) experiments where deuterated electrolyte was used, all potentials were referenced to the reversible hydrogen electrode scale for catalytic activity comparison. Hence, a correction constant (25 mV, as pD = pH × 1.062 due to the difference in pK_W(H) and pK_W(D) (14 vs. 14.87)) was additionally added to the potential in the potential conversion calculation described above[42].

Product quantification

Gas products were analyzed by using an on-line gas chromatograph (GC, SRI Instruments, 8610C) with a thermal conductivity detector and a flame ionization detector. Gas samples were injected into GC every 20 mins and average values over 20, 40, 60 min marks are reported in this study.

For liquid product quantification after electrocatalytic testing in aqueous electrolyte, proton nuclear magnetic resonance (^{1}H NMR, Bruker Avance Neo 500) was used with water suppression. Dimethylsulfoxide (DMSO) with a known concentration was typically used as an internal standard. For deuterated liquid product quantification, deuterium NMR (^{2}H NMR, Bruker Avance Neo 600) was used instead and deuterated DMSO (DMSO-d6) was used as an internal standard.

Faradaic efficiency (FE) of a product was calculated by dividing the amount of charge consumed to produce each product by the total charge passed during CO_2 electrolysis. Reaction products are H_2, CO, formate, and methanol. However, FE for formate after CO_2 electroreduction was trivial (typically less than 0.2%) and thus it is not reported in this work. Total faradaic efficiency normally ranges between 95–100%.

Generation rate of a product ($g_{product}$) was calculated by dividing the product partial current by the Faraday constant and the number of electrons required for product formation from CO_2 (e.g., six for methanol). CO_{int}-to-MeOH conversion (%) was obtained by taking the ratio of MeOH generation rate to CO_{int} generation rate (i.e., $g_{MeOH} / g_{COint} = g_{MeOH} / (g_{CO} + g_{MeOH})$), while CO_{int} selectivity was calculated by dividing the CO_{int} generation rate by total generation rate of all reaction products (CO, MeOH, and H_2) (i.e., $g_{COint} / (g_{CO} + g_{MeOH} + g_{H2})$).

$^{13}CO_2$ electroreduction experiment

$^{13}CO_2$ (99 at.% ^{13}C, 1 L, Sigma-Aldrich) was used to saturate 0.1 M $NaH^{13}CO_3$ (98 at.% ^{13}C, Sigma-Aldrich) electrolyte at 20 sccm for 15 mins prior to $^{13}CO_2$ electrolysis, and the electrolyte was continuously bubbled at 20 sccm during the electrolysis. Due to its limited volume and low pressure (~20 psig), 15-min electrolysis was performed.

Structural characterization

Scanning transmission electron microscopy (STEM) analysis was performed using a probe-aberration corrected Thermo Fisher Scientific Themis Z G3 60-300 kV. High angle annular dark-field (HAADF) STEM images were acquired with a convergence semi-angle of 18.9 mrad operated at 200 kV. Energy dispersive spectroscopy (EDS) elemental maps were collected using a Thermo Fisher Scientific Super-X detector (>0.7 strad collection solid angle). Electron energy loss (EEL) spectra were collected using a Gatan Imaging Filter 1066HR with 0.3 eV/ch energy dispersion. Scanning electron microscopy (SEM) images were obtained using Zeiss Merlin with the in-lens detector.

Density functional theory (DFT) calculation

For a model system, adopted from literature[43], one CoPc molecule was placed above a graphene layer (a total of 98 carbon atoms) at a vertical distance of 15 Å with vacuum between the two structures. All the DFT calculations were conducted using the Vienna Ab initio Simulation Package (VASP)[44,45] with the projector augmented-wave (PAW) approach[46] for the interaction between the ionic core and valence electrons. Electron exchange and correlation were addressed using generalized gradient approximation in the form of the Perdew–Burke–Ernzerhof (PBE) functional, and the D3 method[47] was used for van der Waals dispersion energy-correction. The

ferromagnetic initial state was used in geometry optimization for a consistent and tractable set of magnetic structures. The plane-wave basis set with energy cutoff of 520 eV and a Γ-centered single k-point were used. The energy and force convergence criteria were set to be 10^{-5} eV and 0.05 eV/Å, respectively. We fixed the atomic positions of the graphene layer and the benzene rings of CoPc for better convergence in geometry optimization. We also performed Crystal Orbital Hamilton Populations (COHP)[39] analysis on the Co-C bonding between the cobalt of CoPc and the carbon of adsorbed intermediate species using LOBSTER software (local orbital basis suite towards electronic-structure reconstruction)[48].

The Gibbs free energy (G) of all adsorbed states at 298 K and 1 atm was calculated as follows:

$$G = H - T\Delta S = E_{DFT} + E_{ZPE} + E_{solv} + \int_0^{298} C_v \mathrm{d}T - T\Delta S$$

where E_{DFT} is the electronic total energy calculated from the VASP, E_{ZPE} is the zero-point vibrational energy, and E_{solv} is the solvation energy. The enthalpy ($\int_0^{298} C_v \mathrm{d}T$) and entropy ($\Delta S$) contributions at room temperature were calculated from the vibrational modes of the system (Supplementary Table 1). To determine the solvation corrections (E_{solv}), single-point calculations using the VASPsol solvent model[49] were performed to the relaxed structures. We also applied an energy correction of 0.15 eV per C=O double-bond in the DFT calculations using GGA-PBE functionals[35,50]. The computational hydrogen electrode (CHE) model was used to determine the reaction thermodynamics[51,52].

To account for an electric field induced by electrolyte cations that can lead to notable stabilization of intermediate species[53], we applied external electrostatic field in the z-direction to the adsorbates in vacuum with the solvent model removed[35]. The interaction energy between an adsorbate and an electric field at the interface is obtained by using the following equation[9]:

$$\Delta E = \mu\varepsilon - \frac{1}{2}\alpha\varepsilon^2$$

where ΔE is the change in binding energy, which is calculated by subtracting an adsorption energy in the absence of an electric field (E_0) from a corresponding adsorption energy in the presence of an applied field (E)[9]. ε is the electric field strength, and μ and α are the intrinsic dipole moment and polarizability of the adsorbate, respectively. We used an electric field strength of –1 V/Å to approximate the cation-induced electric field (Supplementary Tables 2 and 3)[9,53].

Classical molecular dynamics (MD) simulations

To elucidate how cations and their vicinal water molecules (i.e., hydration shell) interact with the key reaction intermediate (*CHO) adsorbed on CoPc for electrocatalytic CO_2-to-methanol conversion, we conducted a series of MD simulations of an aqueous electrolyte with alkali cations (Li^+, Na^+, K^+, and Cs^+) confined between two graphene electrodes. Note that due to limited validation of the force field parameters of bicarbonate anions, an equivalent number of chloride anions was considered instead[1], which does not influence our conclusions on the role of cations in methanol production. One CoPc molecule with a CHO intermediate adsorbed on the cobalt single site was placed on top of the bottom graphene layer, and a constant potential of –1.2 V relative to the point of zero charge (PZC) for graphene (0.10 V vs. SHE in pH 6.8 aqueous electrolyte)[54], which corresponds to –0.7 V vs. RHE, was applied. All the simulations were performed using

LAMMPS (large-scale atomic/molecular massively parallel simulator)[55]. We first prepared a simulation box with dimensions of 29.9 Å × 34.5 Å × 24.0 Å, and periodically replicated in the x, y directions while keeping the fixed boundary conditions for the z-direction, containing the graphene electrodes. Each simulation box contained 784 carbon atoms (the graphene electrodes), 800 water molecules, and 18 alkali ions with the equivalent number of chloride anions to achieve charge neutrality. This condition corresponds to ~1 M concentration of cations. The initial configuration of CoPc adsorbed on a graphene layer was adopted from the previous literature[43]. The CoPc-CHO structure was then constructed by adding the CHO on the cobalt site of the CoPc molecule and relaxing the structure using DFT calculations (VASP using GGA-PBE functionals). We used the universal force field (UFF)[56] parameters for the CoPc-CHO complex and built the initial configuration LAMMPS data file for the CoPc-CHO on the graphene layer using the LAMMPS-interface software package[57] (Supplementary Table 6). The charges and the optimized geometries for the CoPc-CHO complex were obtained using the DFT computations using Gaussian16 software package[58] and are listed in Supplementary Table 5. After that, we added water molecules, cations, and anions to the system using the PACKMOL software package[59]. Lorentz-Berthelot mixing rules were employed to derive the mixed Lennard-Jones (LJ) parameters. We used SPC/E (extended simple point-charge model) force field parameters[60] for water molecules, while the graphene electrode atoms were modelled using the LJ force field from UFF parameters (listed in Supplementary Table 4). The charges on each graphene atom were calculated at each time step to satisfy the imposed voltage across the cell (–0.7 V vs. RHE) by the constant potential fix in LAMMPS developed by Wang et al.[61]. All the parameters used are summarized in Supplementary Table 4.

After preparing the initial configurations of the systems, the system was then energy minimized using the steepest descent method for 500 steps followed by 500 steps of conjugate gradient minimization to get rid of any unphysical/bad contacts. The system was then equilibrated for 20 ns under an NVT ensemble before performing the final production runs of 5 ns for analysis with time step of 1 fs. The long-range electrostatic interactions were calculated by using a Particle-mesh Ewald algorithm with a real-space cut off value of 9 Å. An NVT ensemble with Langevin thermostat was employed to keep the system at 300 K. Langevin thermostat was used here as we were only concerned with the statics properties of the system at equilibrium[1]. Also, the Shake algorithm was used to constrain the bonds and angles of SPC/E water. The number density for different species of the simulation box was computed using the LAMMPS module, while the radial distribution functions were computed using the VMD (visual molecular dynamics) software package[62].

Data availability: All data are available within the paper and its Supplementary Information or available from the authors upon reasonable request.

References:

1 Huang, B. et al. Cation- and pH-Dependent Hydrogen Evolution and Oxidation Reaction Kinetics. *JACS Au* **1**, 1674–1687 (2021).

2 Strmcnik, D. et al. The role of non-covalent interactions in electrocatalytic fuel-cell reactions on platinum. *Nat. Chem.* **1**, 466–472 (2009).

3 Shah, A. H. et al. The role of alkali metal cations and platinum-surface hydroxyl in the alkaline hydrogen evolution reaction. *Nat. Catal.* **5**, 923–933 (2022).

4 Monteiro, M. C. O. et al. Absence of CO_2 electroreduction on copper, gold and silver electrodes without metal cations in solution. *Nat. Catal.* **4**, 654–662 (2021).

5 Shin, S.-J. et al. A unifying mechanism for cation effect modulating C1 and C2 productions from CO_2 electroreduction. *Nat. Commun.* **13**, 5482 (2022).

6 Ringe, S. et al. Understanding cation effects in electrochemical CO_2 reduction. *Energy Environ. Sci.* **12**, 3001–3014 (2019).

7 Murata, A. & Hori, Y. Product Selectivity Affected by Cationic Species in Electrochemical Reduction of CO_2 and CO at a Cu Electrode. *Bull. Chem. Soc. Jpn.* **64**, 123–127 (1991).

8 Singh, M. R., Kwon, Y., Lum, Y., Ager, J. W., III & Bell, A. T. Hydrolysis of Electrolyte Cations Enhances the Electrochemical Reduction of CO_2 over Ag and Cu. *J. Am. Chem. Soc.* **138**, 13006–13012 (2016).

9 Chen, L. D., Urushihara, M., Chan, K. & Nørskov, J. K. Electric Field Effects in Electrochemical CO_2 Reduction. *ACS Catal.* **6**, 7133–7139 (2016).

10 Gu, J. et al. Modulating electric field distribution by alkali cations for CO_2 electroreduction in strongly acidic medium. *Nat. Catal.* **5**, 268–276 (2022).

11 Deng, W., Zhang, P., Seger, B. & Gong, J. Unraveling the rate-limiting step of two-electron transfer electrochemical reduction of carbon dioxide. *Nat. Commun.* **13**, 803 (2022).

12 Birdja, Y. Y. et al. Advances and challenges in understanding the electrocatalytic conversion of carbon dioxide to fuels. *Nat. Energy* **4**, 732–745 (2019).

13 Kortlever, R., Shen, J., Schouten, K. J. P., Calle-Vallejo, F. & Koper, M. T. M. Catalysts and Reaction Pathways for the Electrochemical Reduction of Carbon Dioxide. *J. Phys. Chem. Lett.* **6**, 4073–4082 (2015).

14 Nitopi, S. et al. Progress and Perspectives of Electrochemical CO_2 Reduction on Copper in Aqueous Electrolyte. *Chem. Rev.* **119**, 7610–7672 (2019).

15 Wu, Y., Jiang, Z., Lu, X., Liang, Y. & Wang, H. Domino electroreduction of CO_2 to methanol on a molecular catalyst. *Nature* **575**, 639–642 (2019).

16 Boutin, E. et al. Aqueous Electrochemical Reduction of Carbon Dioxide and Carbon Monoxide into Methanol with Cobalt Phthalocyanine. *Angew. Chem. Int. Ed.* **58**, 16172–16176 (2019).

17 Kapusta, S. & Hackerman, N. Carbon Dioxide Reduction at a Metal Phthalocyanine Catalyzed Carbon Electrode. *J. Electrochem. Soc.* **131**, 1511 (1984).

18 Shi, L.-L., Li, M., You, B. & Liao, R.-Z. Theoretical Study on the Electro-Reduction of Carbon Dioxide to Methanol Catalyzed by Cobalt Phthalocyanine. *Inorg. Chem.* **61**, 16549–16564 (2022).

19 Hossain, M. N. et al. Temperature dependent product distribution of electrochemical CO_2 reduction on CoTPP/MWCNT composite. *Appl. Catal. B* **304**, 120863 (2022).

20 Monteiro, M. C. O., Dattila, F., López, N. & Koper, M. T. M. The Role of Cation Acidity on the Competition between Hydrogen Evolution and CO_2 Reduction on Gold Electrodes. *J. Am. Chem. Soc.* **144**, 1589–1602 (2022).

21 Dubouis, N. et al. Tuning water reduction through controlled nanoconfinement within an organic liquid matrix. *Nat. Catal.* **3**, 656–663 (2020).
22 Chang, Q. et al. Metal-Coordinated Phthalocyanines as Platform Molecules for Understanding Isolated Metal Sites in the Electrochemical Reduction of CO_2. *J. Am. Chem. Soc.* **144**, 16131–16138 (2022).
23 Zhang, X. et al. Highly selective and active CO_2 reduction electrocatalysts based on cobalt phthalocyanine/carbon nanotube hybrid structures. *Nat. Commun.* **8**, 14675 (2017).
24 Marcandalli, G., Goyal, A. & Koper, M. T. M. Electrolyte Effects on the Faradaic Efficiency of CO_2 Reduction to CO on a Gold Electrode. *ACS Catal.* **11**, 4936–4945 (2021).
25 Wang, L. et al. Electrochemical Carbon Monoxide Reduction on Polycrystalline Copper: Effects of Potential, Pressure, and pH on Selectivity toward Multicarbon and Oxygenated Products. *ACS Catal.* **8**, 7445–7454 (2018).
26 Corbin, N., Zeng, J., Williams, K. & Manthiram, K. Heterogeneous molecular catalysts for electrocatalytic CO_2 reduction. *Nano Res.* **12**, 2093–2125 (2019).
27 Wuttig, A., Yaguchi, M., Motobayashi, K., Osawa, M. & Surendranath, Y. Inhibited proton transfer enhances Au-catalyzed CO_2-to-fuels selectivity. *Proc. Natl. Acad. Sci. USA* **113**, E4585–E4593 (2016).
28 Yang, Y. et al. Inverse kinetic isotope effects in the oxygen reduction reaction at platinum single crystals. *Nat. Chem.* **15**, 271–277 (2022).
29 Warburton, R. E., Soudackov, A. V. & Hammes-Schiffer, S. Theoretical Modeling of Electrochemical Proton-Coupled Electron Transfer. *Chem. Rev.* **122**, 10599–10650 (2022).
30 Liu, Y. & McCrory, C. C. L. Modulating the mechanism of electrocatalytic CO_2 reduction by cobalt phthalocyanine through polymer coordination and encapsulation. *Nat. Commun.* **10**, 1683 (2019).
31 Han, N. et al. Supported Cobalt Polyphthalocyanine for High-Performance Electrocatalytic CO_2 Reduction. *Chem* **3**, 652–664 (2017).
32 Shinagawa, T., Garcia-Esparza, A. T. & Takanabe, K. Insight on Tafel slopes from a microkinetic analysis of aqueous electrocatalysis for energy conversion. *Sci. Rep.* **5**, 13801 (2015).
33 Holewinski, A. & Linic, S. Elementary Mechanisms in Electrocatalysis: Revisiting the ORR Tafel Slope. *J. Electrochem. Soc.* **159**, H864 (2012).
34 Hori, Y., Takahashi, R., Yoshinami, Y. & Murata, A. Electrochemical Reduction of CO at a Copper Electrode. *J. Phys. Chem. B* **101**, 7075–7081 (1997).
35 Liu, X. et al. pH effects on the electrochemical reduction of $CO_{(2)}$ towards C_2 products on stepped copper. *Nat. Commun.* **10**, 32 (2019).
36 Boutin, E., Salamé, A., Merakeb, L., Chatterjee, T. & Robert, M. On the Existence and Role of Formaldehyde During Aqueous Electrochemical Reduction of Carbon Monoxide to Methanol by Cobalt Phthalocyanine. *Chem. Eur. J.* **28**, e202200697 (2022).
37 Shen, J. et al. Electrocatalytic reduction of carbon dioxide to carbon monoxide and methane at an immobilized cobalt protoporphyrin. *Nat. Commun.* **6**, 8177 (2015).
38 Goyal, A. & Koper, M. T. M. The Interrelated Effect of Cations and Electrolyte pH on the Hydrogen Evolution Reaction on Gold Electrodes in Alkaline Media. *Angew. Chem. Int. Ed.* **60**, 13452–13462 (2021).

39 Deringer, V. L., Tchougréeff, A. L. & Dronskowski, R. Crystal Orbital Hamilton Population (COHP) Analysis As Projected from Plane-Wave Basis Sets. *J. Phys. Chem. A* **115**, 5461–5466 (2011).
40 Cao, P. et al. Metal single-site catalyst design for electrocatalytic production of hydrogen peroxide at industrial-relevant currents. *Nat. Commun.* **14**, 172 (2023).
41 Huang, B. et al. Cation-Dependent Interfacial Structures and Kinetics for Outer-Sphere Electron-Transfer Reactions. *J. Phys. Chem. C* **125**, 4397–4411 (2021).
42 Krężel, A. & Bal, W. A formula for correlating pKa values determined in D_2O and H_2O. *J. Inorg. Biochem.* **98**, 161–166 (2004).
43 Choi, C. et al. Efficient electrocatalytic valorization of chlorinated organic water pollutant to ethylene. *Nat. Nanotech.* **18**, 160–167 (2023).
44 Kresse, G. & Hafner, J. Ab initio molecular dynamics for liquid metals. *Phys. Rev. B* **47**, 558–561 (1993).
45 Kresse, G. & Furthmüller, J. Efficient iterative schemes for ab initio total-energy calculations using a plane-wave basis set. *Phys. Rev. B* **54**, 11169–11186 (1996).
46 Blöchl, P. E. Projector augmented-wave method. *Phys. Rev. B* **50**, 17953–17979 (1994).
47 Johnson, E. R. & Becke, A. D. A post-Hartree-Fock model of intermolecular interactions: Inclusion of higher-order corrections. *J. Chem. Phys.* **124**, 174104 (2006).
48 Maintz, S., Deringer, V. L., Tchougréeff, A. L. & Dronskowski, R. LOBSTER: A tool to extract chemical bonding from plane-wave based DFT. *J. Comput. Chem.* **37**, 1030–1035 (2016).
49 Mathew, K., Sundararaman, R., Letchworth-Weaver, K., Arias, T. A. & Hennig, R. G. Implicit solvation model for density-functional study of nanocrystal surfaces and reaction pathways. *J. Chem. Phys.* **140**, 084106 (2014).
50 Christensen, R., Hansen, H. A. & Vegge, T. Identifying systematic DFT errors in catalytic reactions. *Catal. Sci. Technol.* **5**, 4946–4949 (2015).
51 Nørskov, J. K. et al. Origin of the Overpotential for Oxygen Reduction at a Fuel-Cell Cathode. *J. Phys. Chem. B* **108**, 17886–17892 (2004).
52 Peterson, A. A., Abild-Pedersen, F., Studt, F., Rossmeisl, J. & Nørskov, J. K. How copper catalyzes the electroreduction of carbon dioxide into hydrocarbon fuels. *Energy Environ. Sci.* **3**, 1311–1315 (2010).
53 Resasco, J. et al. Promoter Effects of Alkali Metal Cations on the Electrochemical Reduction of Carbon Dioxide. *J. Am. Chem. Soc.* **139**, 11277–11287 (2017).
54 Poon, J., Batchelor-McAuley, C., Tschulik, K. & Compton, R. G. Single graphene nanoplatelets: capacitance, potential of zero charge and diffusion coefficient. *Chem. Sci.* **6**, 2869–2876 (2015).
55 Thompson, A. P. et al. LAMMPS - a flexible simulation tool for particle-based materials modeling at the atomic, meso, and continuum scales. *Comput. Phys. Commun.* **271**, 108171 (2022).
56 Rappe, A. K., Casewit, C. J., Colwell, K. S., Goddard, W. A., III & Skiff, W. M. UFF, a full periodic table force field for molecular mechanics and molecular dynamics simulations. *J. Am. Chem. Soc.* **114**, 10024–10035 (1992).
57 Boyd, P. G., Moosavi, S. M., Witman, M. & Smit, B. Force-Field Prediction of Materials Properties in Metal-Organic Frameworks. *J. Phys. Chem. Lett.* **8**, 357–363 (2017).
58 Frisch, M. J. et al. *Gaussian 16 Rev. C.01*, Gaussian, Inc., Wallingford CT (2016).

59 Martínez, L., Andrade, R., Birgin, E. G. & Martínez, J. M. PACKMOL: A package for building initial configurations for molecular dynamics simulations. *J. Comput. Chem.* **30**, 2157–2164 (2009).
60 Berendsen, H. J. C., Grigera, J. R. & Straatsma, T. P. The missing term in effective pair potentials. *J. Phys. Chem.* **91**, 6269–6271 (1987).
61 Wang, Z., Yang, Y., Olmsted, D. L., Asta, M. & Laird, B. B. Evaluation of the constant potential method in simulating electric double-layer capacitors. *J. Chem. Phys.* **141**, 184102 (2014).
62 Humphrey, W., Dalke, A. & Schulten, K. VMD: Visual molecular dynamics. *J. Mol. Graph.* **14**, 33–38 (1996).

Author Information

Corresponding Author:

Sunmoon Yu; Email: sunmoon@mit.edu

Yang Shao-Horn; Email: shaohorn@mit.edu

Competing interests:

The authors declare no competing financial interest.

Acknowledgments:

This work was supported by Niterra Co., LTD. The authors are grateful to W. Massefski, J. Grimes, and B. Adams for their assistance with NMR pulse sequence optimization and data analysis. We thank J. Johnson, A. Wang, and B. Liu for access to their freeze dryer. We also thank J. Peng and J. Lunger for discussions on our computational approaches. This work used the Extreme Science and Engineering Discovery Environment, which is supported by National Science Foundation grant number DMR-160163. The authors also acknowledge the MIT SuperCloud and Lincoln Laboratory Supercomputing Center for providing HPC resources.

Author contributions: S.Y. and Y.S.-H conceived the research idea. S.Y. and H.Y. performed experiments with assistance from H.X. and D.J.Z. S.W. and A.A. carried out DFT calculations and MD simulations, respectively. J.K. conducted electron microscopy characterization. B.H., H.X., D.J.Z., X.W., H.I., and D.M. contributed to the discussions. S.Y. and Y.S.-H wrote the manuscript with feedback from all authors.

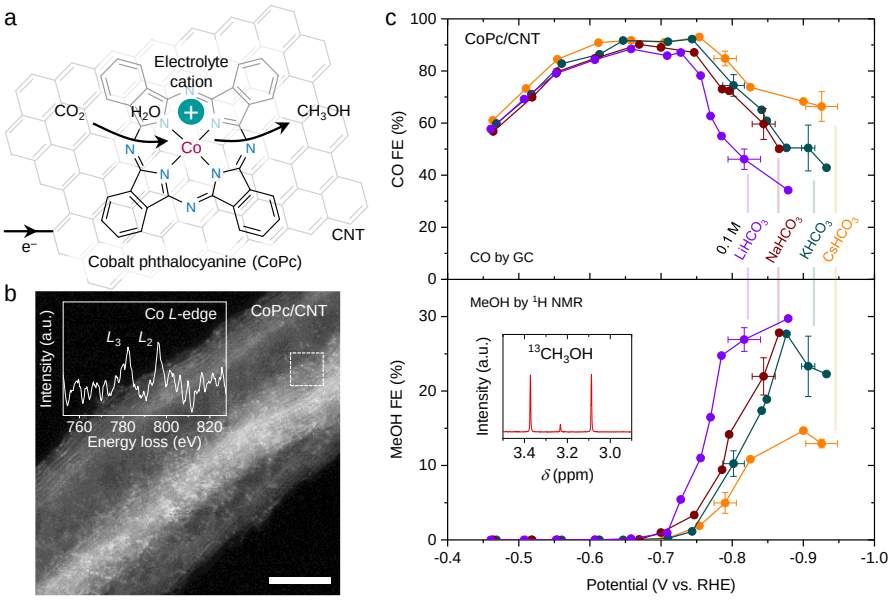

Fig. 1. Electrocatalytic CO_2-to-methanol conversion by cobalt phthalocyanine catalyst supported on carbon nanotube (CoPc/CNT) and its cation dependence. a, Schematic of CoPc/CNT with an electrolyte cation in the vicinity of the cobalt active site. **b**, High-angle annular dark-field scanning transmission electron microscopy (HAADF-STEM) image of CoPc/CNT (scale bar: 5 nm). The inset in **b** shows an electron energy loss spectrum obtained from the dashed area. **c**, Faradaic efficiencies (FEs) for CO_2RR products: carbon monoxide (CO, top) and methanol (MeOH, bottom). The inset in **c** shows a proton nuclear magnetic resonance (^{1}H NMR) spectrum after $^{13}CO_2$ reduction experiment. Electrochemical testing was conducted in a typical H-cell where cathodic and anodic compartments are separated by an anion exchange membrane. Gas and liquid reaction products were quantified using gas chromatography (GC) and NMR, respectively. Error bars are one standard deviation of at least three independent measurements.

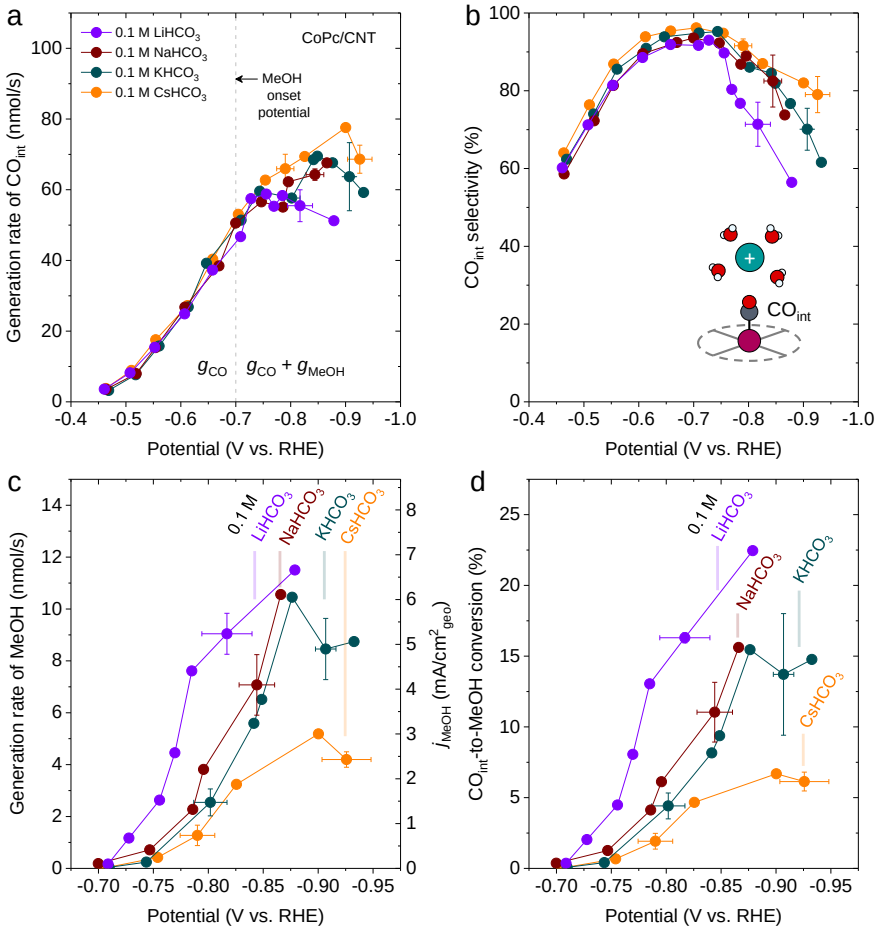

Fig. 2. Effect of electrolyte cation on CO intermediate (CO_{int}) generation rate and CO_2-to-methanol conversion of CoPc/CNT. a,**b**, CO_{int} generation rate (**a**) and CO_{int} selectivity (**b**) in bicarbonate electrolytes with different cations. Generation rates were calculated by dividing product partial currents by the Faraday constant and the number of electrons needed for the product formation. The CO_{int} generation rates were derived from generation rates of CO (g_{CO}) and methanol (g_{MeOH}). CO_{int} selectivity was obtained from the ratio of the CO_{int} generation rate to total generation rate of all products. The vertical dashed gray line at –0.7 V vs. RHE in (**a**) indicates the onset potential for methanol formation. The schematic in (**b**) describes the formation of CO_{int} on CoPc catalyst (cyan: electrolyte cation, red: oxygen, white: hydrogen, gray: carbon, magenta: cobalt). **c**,**d**, Generation rate of methanol (**c**, left y-axis), methanol partial current density (**c**, right y-axis), and CO_{int}-to-MeOH conversion (**d**) with different electrolyte cations. The CO_{int}-to-MeOH conversion was calculated from the g_{MeOH}/g_{COint} ratio. Error bars are one standard deviation of at least three independent measurements.

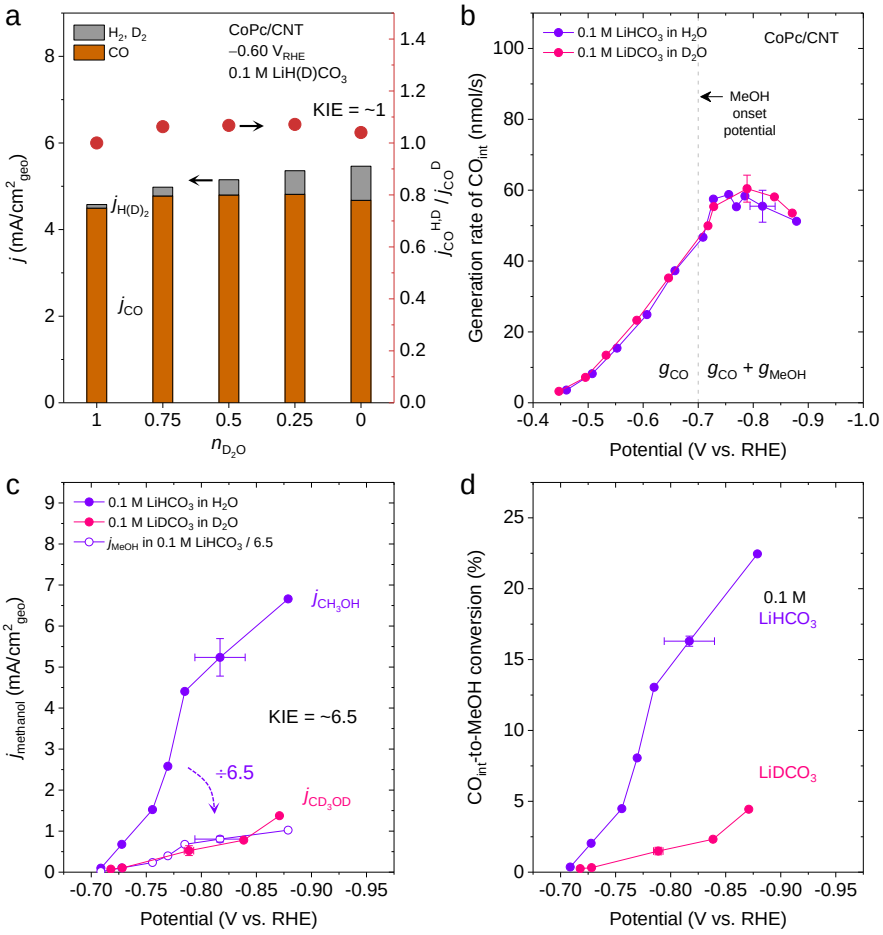

Fig. 3. Kinetic isotope effect (KIE) on CO_2-to-CO and CO_2-to-methanol conversions. a, Partial current density for CO and $H(D)_2$ (left y-axis), and KIE value for CO production (right y-axis) at –0.6 V vs. RHE as a function of D_2O fraction (n_{D2O}) in D_2O-H_2O mixture solution. **b-d**, CO_{int} generation rates (**b**), methanol partial current densities (**c**), and CO_{int}-to-methanol conversion (**d**) of CoPc/CNT in 0.1 M $LiHCO_3$ and $LiDCO_3$. Error bars are one standard deviation of at least three independent measurements.

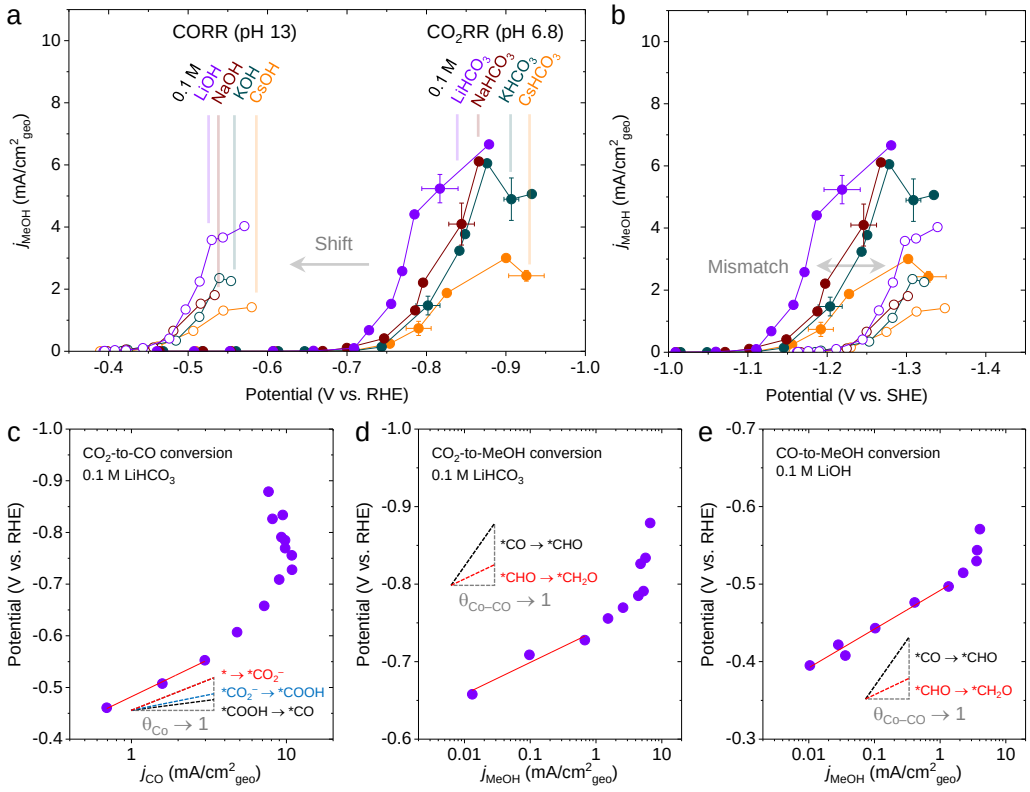

Fig. 4. Comparison in electrocatalytic CO_2- and CO-to-methanol conversions by CoPc/CNT and Tafel analyses. a,**b**, Methanol partial current densities under CO (void symbols) and CO_2 (solid symbols) reduction reaction conditions (CORR and CO_2RR, respectively) as a function of potential on the RHE (**a**) and the SHE (**b**) scales. For CORR, hydroxide electrolyte (pH 13) was used, while bicarbonate electrolyte (pH 6.8) for CO_2RR. The gray arrows in **a** and **b** indicate positive potential shifts and potential mismatches on the RHE and SHE scales, respectively. **c-e**, Tafel plots for CO_2RR (**c** and **d**) and CORR (**e**) conditions. Tafel slopes having different rate-determining steps (RDSs) and assumptions (θ_{Co} denotes the intermediate species coverage of the cobalt site) are indicated in the inset (red: proposed RDSs in this study, blue and black: possible alternative RDSs). Error bars are one standard deviation of at least three independent measurements.

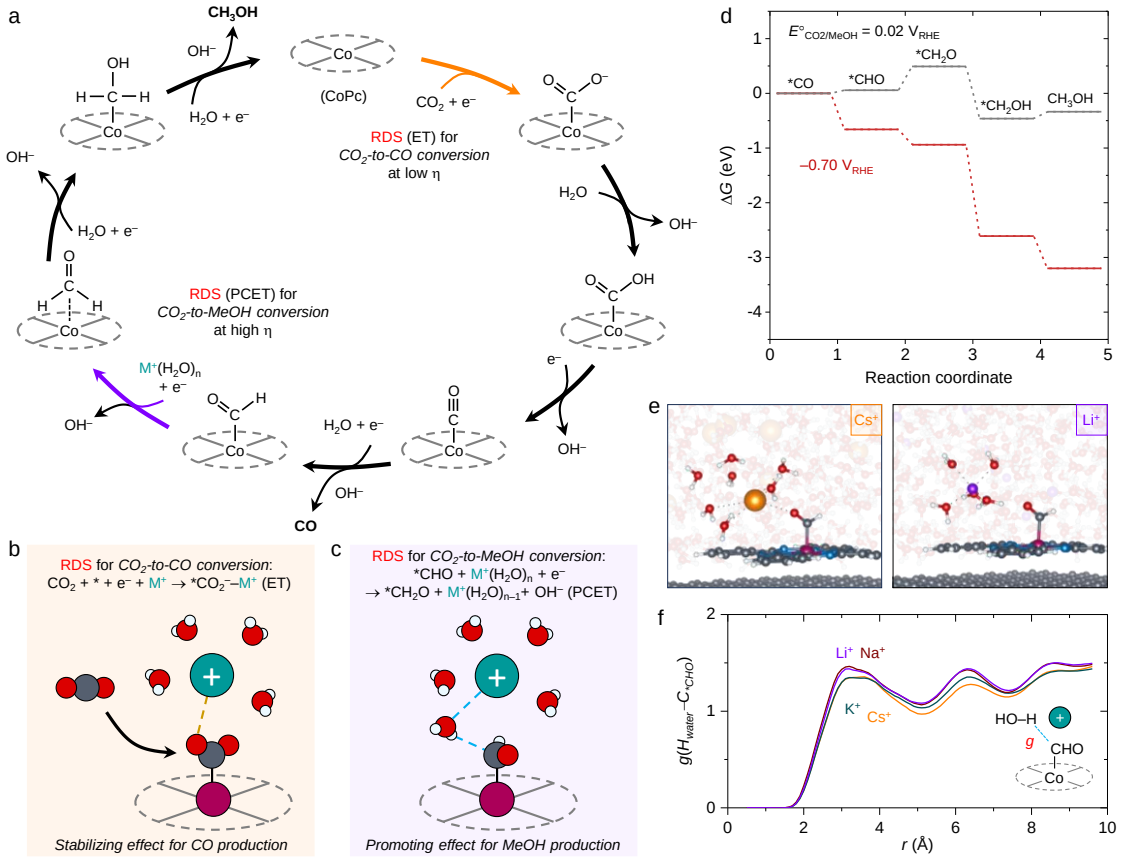

Fig. 5. Proposed mechanistic pathways for electrochemical CO_2-to-CO and CO_2-to-methanol conversions catalyzed by CoPc and roles of cations in the respective reactions. a, Overall catalytic cycle of CoPc catalyst during CO_2 electroconversion. **b**,**c**, Schematics describing rate-determining steps (RDSs) and roles of cations. The RDS for CO_2-to-CO conversion at low overpotentials (η) is an electron transfer (ET) to CO_2 molecule (**b**), while the RDS for CO_2-to-methanol conversion at high overpotentials is the protonation of *CHO intermediate through a proton-coupled electron transfer (PCET) (**c**). The dashed brown line in (**b**) indicates electrostatic interaction between cation and adsorbed intermediate species, while the dashed blue line in (**c**) represents non-covalent interaction between intermediate species and vicinal water molecules in the cation hydration shell (cyan: electrolyte cation, red: oxygen, white: hydrogen, gray: carbon, magenta: cobalt). **d**, Density functional theory (DFT) free energy diagram of the proposed reaction pathway from *CO to methanol at 0.02 V_{RHE} (equilibrium potential for CO_2-to-methanol reduction) and –0.7 V_{RHE}. **e**, Representative snapshots from molecular dynamics simulations showing different solvation structures near the cation (Cs^+ and Li^+, left and right, respectively) and the adsorbed CHO intermediate. **f**, Radial distribution function (g) of H_{water}–C_{*CHO} (depicted in the inset) for different cations.